Short- and Long-Range Orbital Order in Phase Separated $Pr_{0.50}Ca_{0.50}Mn_{0.99}Ti_{0.01}O_3$: Its Role in Thermal Hysteresis

C. Frontera,*[,†] J. L. García-Muñoz,[†] P. Beran,[†] N. Bellido,[†,‡] I. Margiolaki,[§] and C. Ritter[||]

Institut de Ciencia de Materials de Barcelona, CSIC, Campus Universitari de Bellaterra, 08193 Bellaterra, Spain, Laboratoire CRISMAT, UMR 6508 CNRS/Ensicaen, 6 bd du Maréchal Juin, F-14050 Caen Cedex, France, European Synchrotron Radiation Facility, 6, rue Jules Horowitz, F-38042 Grenoble Cedex 9, France, and Institut Laue Langevin, 6, rue Jules Horowitz, F-38042 Grenoble Cedex 9, France

Received December 10, 2007. Revised Manuscript Received February 11, 2008

By means of high resolution synchrotron X-ray and neutron powder diffraction we have investigated the structural evolution of $Pr_{0.50}Ca_{0.50}Mn_{0.99}Ti_{0.01}O_3$. We have found two structural transitions on cooling; the first takes place at $T_{CO} \simeq 240$ K and the second in a wide temperature range around 100−140 K. Below the first transition two phases coexist; one presents robust charge/orbital ordering, characterized by strong lattice distortions and low strain, and the second presents charge/orbital order characterized by smaller lattice distortions with remarkable spatial fluctuations and short ranged orbital ordering. This second phase is metastable giving rise to thermal hysteresis of structural and macroscopic properties in the cooling−heating cycle. We have observed that thermal hysteresis is due to (i) the transformation of a huge region of short-ranged order into long-ranged ordered regions and (ii) a hardening of the remaining short-ranged regions in which the lattice distortion grows and the strain diminishes. We also report a detailed characterization of the low temperature (ground state) coexisting phases including their structural details, ordered magnetic structures, coherence lengths, microstructural details, and so forth. A great degree of magnetic disorder characterizes the low temperature ground state of the investigated highly diluted manganite.

1. Introduction

Since the description of magnetoresistance in manganites,[1] physics of these oxides has attracted the attention of many research groups during the last 14 years. This phenomenon has been found to be directly related to the coexistence of a paramagnetic-insulating phase and a ferromagnetic and metallic phase that is tailored by the external magnetic field.[2] Phase separation/coexistence is nowadays one of the hottest topics in the study of manganites and it gives rise to a series of spectacular and technologically interesting behaviors of these compounds. Among others are the appearance of persistent magnetoresistive memory;[3,4] the appearance of ultrasharp steps (avalanches) in the low temperature resistivity, magnetization, and specific heat isothermal curves under magnetic field;[5,6] and so forth.

This last effect has been extensively studied in Mn-substituted half-doped manganites like $Pr_{0.50}Ca_{0.50}Mn_{1-x}M_x$ (M ≡ Co, Ni, Fe, Ti, Ga, etc.).[5–14] Different appealing phenomena have been reported in these compounds. For some substituting cations, the charge/orbital order (COO) insulating phase present in the parent $Pr_{0.50}Ca_{0.50}MnO_3$ compound is lost with low levels (3−5%) of Mn substitution.[7–10] It has been suggested that the magnetic behavior of these compounds is determined by the electronic structure of the substituting ions. Ions with active d-electrons rapidly destroy COO and turn the low temperature antiferromagnetic (AFM) order ferromagnetic (FM), but apparently ions without active d-electrons would not induce FM order.[10] Besides, the substitution level seems to be a key parameter, and its role has not been yet clarified. For instance, low (2%) substitution

[†] CSIC.
[‡] UMR 6508 CNRS/Ensicaen.
[§] European Synchrotron Radiation Facility.
[||] Institut Laue Langevin.

(1) von Helmolt, R.; Wecker, J.; Holzapfel, B.; Schultz, L.; Samwer, K. *Phys. Rev. Lett.* **1993**, *71*, 2331.
(2) Uehara, M.; Mori, S.; Chen, C.; Cheong, S. *Nature* **1999**, *399*, 560.
(3) Levy, P.; Parisi, F.; Granja, L.; Indelicato, E.; Polla, G. *Phys. Rev. Lett.* **2002**, *89*, 137001.
(4) Levy, P.; Parisi, F.; Quintero, M.; Granja, L.; Curiale, J.; Sacanell, J.; Leyva, G.; Polla, G.; Freitas, R. S.; Ghivelder, L. *Phys. Rev. B* **2002**, *65*, 140401(R).
(5) Mahendiran, R.; Maignan, A.; Hébert, S.; Martin, C.; Hervieu, M.; Raveau, B.; Mitchell, J. F.; Schiffer, P. *Phys. Rev. Lett.* **2002**, *89*, 286602.
(6) Hébert, S.; Hardy, V.; Maignan, A.; Mahendiran, R.; Hervieu, M.; Martin, C.; Raveau, B. *J. Solid State Chem.* **2002**, *165*, 6.
(7) Raveau, B.; Maignan, A.; Martin, C. *J. Solid State Chem.* **1997**, *130*, 162–166.
(8) Toulemonde, O.; Studer, F.; Raveau, B. *Solid State Commun.* **2001**, *118*, 107–112.
(9) Hébert, S.; Maignan, A.; Frésard, R.; Hervieu, M.; Retoux, R.; Martin, C.; Raveau, B. *Eur. Phys. J. B* **2001**, *24*, 85–89.
(10) Hébert, S.; Maignan, A.; Martin, C.; Raveau, B. *Solid State Commun.* **2002**, *121*, 229–234.
(11) Yaicle, C.; Frontera, C.; García-Munoz, J. L.; Martin, C.; Maignan, A.; Andrée, G.; Bourée, F.; Ritter, C.; Margiolaki, I. *Phys. Rev. B* **2006**, *74*, 144406.
(12) Damay, F.; Martin, C.; Maignan, A.; Hervieu, M.; Raveau, B.; Boureé, F.; Andreé, G. *Appl. Phys. Lett.* **1998**, *73*, 3772.
(13) Yaicle, C.; Martin, C.; Jirak, Z.; Fauth, F.; André, G.; Suard, E.; Maignan, A.; Hardy, V.; Retoux, R.; Hervieu, M.; Hébert, S.; Raveau, B.; Simon, Ch.; Saurel, D.; Brûlet, A.; Bourée, F. *Phys. Rev. B* **2003**, *68*, 224412.
(14) Yaicle, C.; Fauth, F.; Martin, C.; Retoux, R.; Jirak, Z.; Hervieu, M.; Raveau, B.; Maignan, A. *J. Solid State Chem.* **2005**, *178*, 1652–1660.

10.1021/cm703513t CCC: $40.75
Published on Web 04/15/2008

with Co (with active d-electrons) drives the coexistence of two AFM phases as recently reported,[11] although 5% Co substitution drives the apparition of long-range FM order. It is important to recall that despite the fact that some phenomena solely occur in the low dilution limit ($x \leq 1-2\%$) detailed studies in the range of low doping are very scarce.

Detailed structural characterization of these systems ($Pr_{0.50}Ca_{0.50}Mn_{1-x}M_xO_3$) in the region of moderated substitution ($2\% \leq x \leq 5\%$) prove the presence of two phases in all the studied cases.[11–14] Recently, the important role of the strain for the stabilization of the coexisting phases has been evidenced for these systems in particular (see refs 11 and 14) and for some nonsubstituted manganites (for instance, refs 15 and 16). From results in refs 11 and 14 one can infer that the phase separation in $Pr_{0.50}Ca_{0.50}Mn_{1-x}M_xO_3$ gives rise to the coexistence of two differently distorted phases at low temperature and to the accommodation of huge strain in the less distorted structural phase. It must be mentioned that the introduction of impurities in the Mn sublattice can induce differences in the Mn^{3+}/Mn^{4+} ratios in the coexisting phases.

This work is focused on lowly doped $Pr_{0.50}Ca_{0.50}Mn_{0.99}Ti_{0.01}O_3$ with mainly two objectives. The first is to investigate the exclusive properties of the low doping extreme and the novel features that we have found to occur in this compound. The second is to progress in our understanding of the relevance of strain fields for phase separation phenomena in manganites. Key properties of the Ti substitution are that (i) Ti^{4+} ions do not have unpaired d electrons [d^0] able to promote large FM-metallic regions. (ii) The empty d shell makes this substitution nonmagnetic. On the other hand this substitution favors an excess of Mn^{3+} in the system. Hence, Ti introduces random disorder without introducing Mn−Ti magnetic interactions. The reason for choosing the composition with $x = 1\%$ is because we consider the low-doping limit the most suitable for studying the relevance of microstrain in the phase segregation of these oxides. In this low doping region, it can be expected that the study of the effect of isolated, rather than interconnected, impurities will be more feasible.

Sample preparation and some experimental details concerning synchrotron and neutron data collection and analysis are given in section 2. In subsection 3.1 the transport and magnetic measurements are presented, giving special emphasis to the temperature and field anomalies and thermal hysteresis effects. Subsections 3.2 and 3.3 are devoted to a careful structural investigation of segregated phases and their temperature evolution which includes a microstructural study of the different domains based on the profile shapes in the diffraction patterns. Details about the magnetic order/disorder are given in subsection 3.4. In section 4 the conclusions of the work are presented.

2. Experimental Details

Polycrystalline samples of $Pr_{0.50}Ca_{0.50}Mn_{1-x}Ti_xO_3$ ($0.01 \leq x \leq 0.05$) were prepared following standard solid-state reaction methods, from the intimate mixture of stoichiometric weights of high purity Pr_6O_{11}, $CaCO_3$, Mn_2O_3, and TiO_2. After intermediate heat treatments the powders were pressed into pellets at 10 tons and heated up to 1400 °C several times with intermediate grindings. The purity and crystallinity of the final products were studied by X-ray powder diffraction. We found that the compounds were well crystallized and free from impurities up to the detection limit of the technique (∼1 wt %).

Structural characterization of $Pr_{0.50}Ca_{0.50}Mn_{0.99}Ti_{0.01}O_3$ has been done by means of neutron and synchrotron X-ray powder diffraction (NPD and SXRPD). NPD data were collected at 5 and 300 K on a high resolution D2B [$\lambda = 1.594$ Å] neutron diffractometer of ILL (Grenoble, France). SXRPD data were taken on a ultrahigh resolution ID31 diffractometer ($\lambda = 0.500111(12)$ Å) of the ESRF (Grenoble, France) at different temperatures. The short wavelength, to reduce the absorption, was selected with a double-crystal Ge(111) monochromator and calibrated with Si NIST ($a = 5.43094$ Å). Optimum transmission was achieved by enclosing the finely grounded sample in a 0.5 mm diameter borosilicate glass capillary, and appropriate spinning of the capillary in the beam ensured for a good powder averaging. Low temperature patterns were recorded placing the capillary in a continuous liquid-helium flow cryostat with rotating sample rod. All diffraction data were analyzed by the Rietveld method using the FullProf package.[17] To obtain confident microstructural information of measured samples, we have first determined the contribution to the profile shape function coming from the diffractometer. This has been achieved by measuring well crystallized $Na_2Ca_3Al_2F_{14}$, with a negligible sample contribution.[18] The contribution coming from the samples has been analyzed following the Stephens' formalism implemented in FullProf 2000 program.[19,20] According to this formalism, the contribution to the broadening of (*hkl*) reflection, σ_{hkl}, due to the strain reads

$$\sigma_{hkl}{}^2 = \sum_{\substack{H,K,L\geq 0 \\ H+K+L=4}} S_{HKL} h^H k^K l^L \qquad (1)$$

where S_{HKL} are adjustable parameters related to the fluctuation of distances between crystallographic planes and their correlations. For an orthorhombic cell, only six terms of this sum are different from zero:

$$\sigma_{hkl}{}^2 = S_{400}h^4 + S_{040}k^4 + S_{004}l^4 + S_{220}h^2k^2 + S_{202}h^2l^2 + S_{022}k^2l^2 \qquad (2)$$

A SQUID magnetometer (Quantum Design) was used for magnetization measurements. For DC magnetotransport data (measured by the four probes method) we used a commercial PPMS system (Quantum Design), and data was taken in the $2\text{ K} \leq T \leq 300\text{ K}$ temperature range.

3. Results and Discussion

3.1. Magnetization and Transport Properties. Figure 1a shows the thermal evolution of the magnetization of $Pr_{0.50}Ca_{0.50}Mn_{0.99}Ti_{0.01}O_3$ measured under a magnetic field of 0.1 T. The three curves shown correspond to measurements done (i) on heating after zero field cooling (ZFC); (ii) on cooling under field; and (iii) on heating after field cooling (FC). At about $T_{CO} \simeq 240$ K a broad maximum in $M(T)$

(15) Lookman, T.; Bishop, A. *Nature* **2004**, *428*, 401–404.
(16) Sagdeo, P. R.; Anwar, S.; Lalla, N. P. *Phys. Rev. B* **2006**, *74*, 214118.
(17) Rodríguez-Carvajal, J. *Physica B* **1993**, *192*, 55.
(18) Masson, O.; Dooryhée, E.; Cheary, R. W.; Fitch, A. N. *Mater. Sci. Forum* **2001**, *378−381*, 300–305.
(19) Rodríguez-Carvajal, J.; Fernández-Díaz, M. T.; Martínez, J. L. *J. Phys. Condens. Matter* **1991**, *3*, 3215.
(20) Stephens, P. W. *J. Appl. Crystallogr.* **1999**, *32*, 281.

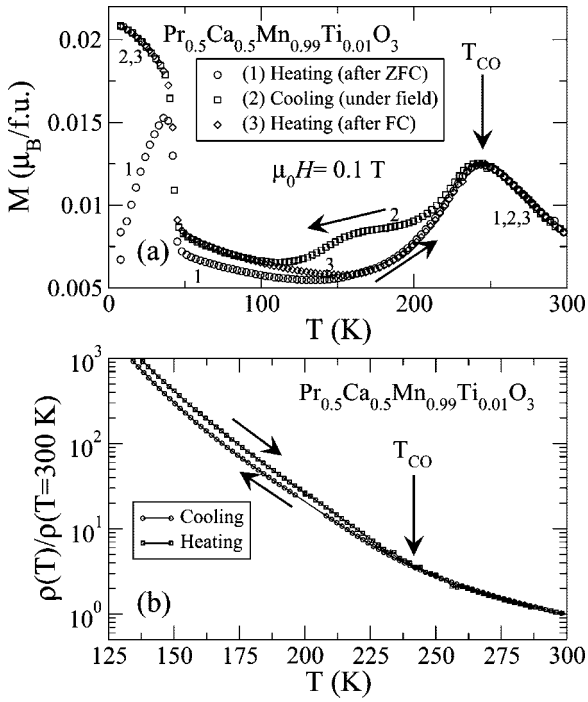

Figure 1. (a) Dependence on temperature of DC magnetization taken under an applied field of $\mu_0 H = 0.1$ T during heating and cooling processes as indicated by the arrows. (b) Resistivity normalized to that measured at 300 K during heating and cooling processes. The resistivity grows rapidly below 125 K.

curves is clearly visible. This maximum is also found in the pristine $Pr_{0.50}Ca_{0.50}MnO_3$ compound at the same temperature and corresponds to the COO transition. Above T_{CO} the three curves displayed perfectly match. On the contrary, below this temperature, clear differences between the magnetization measured on cooling and that measured on heating (both ZFC and FC) appear, the former being higher than the latter. These differences persist for about 150 K disappearing at $T \cong 100$ K. Below 100 K, the two curves measured on cooling and heating (FC) under field match again perfectly. The differences found cannot be described as a simple displacement of the charge ordering transition and deserve some attention. The reduction of the magnetization shown in Figure 1a, below T_{CO}, is due to the substitution of the FM correlations between Mn moments, existing above T_{CO}, by the AFM correlations present below T_{CO}. It is apparent from Figure 1a that this change takes place in two steps during the cooling process while the inverse change, during the heating process (FC and ZFC), takes place in a unique step giving rise to this remarkable hysteresis (cooling and heating under field). In addition after this second transition in the cooling process, which takes place between 150 K and 100 K, the differences between cooling and heating curves disappear. The existence of hysteresis on the cooling−heating cycle has been previously reported in different pure manganites[21,22] and also in

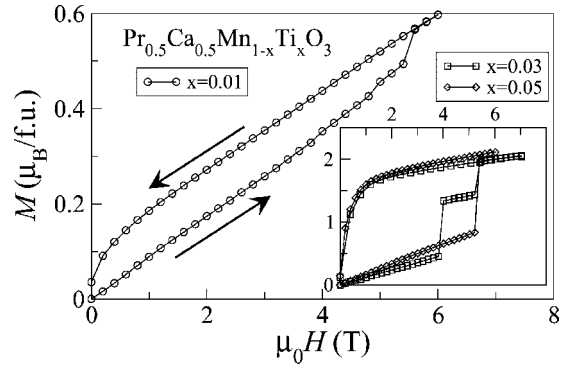

Figure 2. Isothermal magnetization vs field at low temperature (2 K) measured for $Pr_{0.50}Ca_{0.50}Mn_{0.99}Ti_{0.01}O_3$. For comparison, the inset shows data for $Pr_{0.50}Ca_{0.50}Mn_{1-x}Ti_xO_3$ with $x = 0.03$ and 0.05.

Mn-substituted ones.[23,24] Interestingly, the case of $Pr_{0.50}Ca_{0.50}Mn_{0.99}Ti_{0.01}O_3$ is very similar to that presented here (magnetization on cooling is higher than on heating),[23] although Cr^{3+} ions have active d-electrons (d^3) in contrast with Ti^{4+} (d^0). We highlight here that this two-step transition and the thermal hysteresis is reproducible: samples prepared in different batches present the same behavior.

We have also found a hysteretic behavior in the resistivity, as Figure 1b shows: when cooling-down the compound its resistivity curve remains lower than when heating up. At temperatures below those shown in Figure 1b the resistivity increases continuously (the sample becomes, at low temperature, too resistive and we failed on measuring its resistance below 80 K). We did also try to measure the low temperature ($T = 2$ K) resistivity under applied field, but it was too high even under 6.5 T of applied field. In accordance with magnetization measurements, the charge ordering transition is more visible on heating than on cooling.

At lower temperatures, below 50 K, magnetization curves in Figure 1a show some interesting features. First, there is a clear anomaly in magnetization curves at $T_G \simeq 45$ K. At this temperature the ZFC curve presents a pronounced cusp (on heating), but it does not join the FC curve. On the contrary, the differences between ZFC and FC curves extend up to about $T \simeq 160$ K. This signals the existence of magnetic disorder in our system that must be ascribed to the random substitution of magnetic Mn atoms at the Mn^{3+} or Mn^{4+} sites ions by nonmagnetic Ti^{4+}. The behavior described here is very similar to that reported for $Pr_{0.50}Ca_{0.50}Mn_{0.975}Al_{0.025}O_3$.[25] Authors in ref 25 discuss some possibilities for this effect and conclude that the origin of the transition found at low temperature is the blocking of the magnetic domains due to the quenched disorder.

Figure 2 shows the isothermal magnetization of $Pr_{0.50}Ca_{0.50}Mn_{0.99}Ti_{0.01}O_3$ versus the applied magnetic field measured at 2 K. For the sake of comparison, the curves for $Pr_{0.50}Ca_{0.50}Mn_{1-x}Ti_xO_3$ with $x = 0.03$ and 0.05 are also plotted in the inset. These curves show that the Ti-substituted family presents field-induced magnetization steps at low temperature

(21) Ghivelder, L.; Freitas, R. S.; das Virgens, M. G.; Continentino, M. A.; Martinho, H.; Granja, L.; Quintero, M.; Leyva, G.; Levy, P.; Parisi, F. *Phys. Rev. B* **2004**, *69*, 214414.
(22) Fisher, L. M.; Kalinov, A. V.; Voloshin, I. F.; Babushkina, N. A.; Khomskii, D. I.; Zhang, Y.; Palstra, T. T. M. *Phys. Rev. B* **2004**, *70*, 212–411.
(23) Mahendiran, R.; Maignan, A.; Hervieu, M.; Martin, C.; Raveau, B. *J. Solid State Chem.* **2001**, *160*, 1–3.
(24) Banerjee, A.; Mukherjee, K.; Kumar, K.; Chaddah, P. *Phys. Rev. B* **2006**, *74*, 224445.
(25) Nair, S.; Banerjee, A. *Phys. Rev. Lett.* **2004**, *93*, 117204.

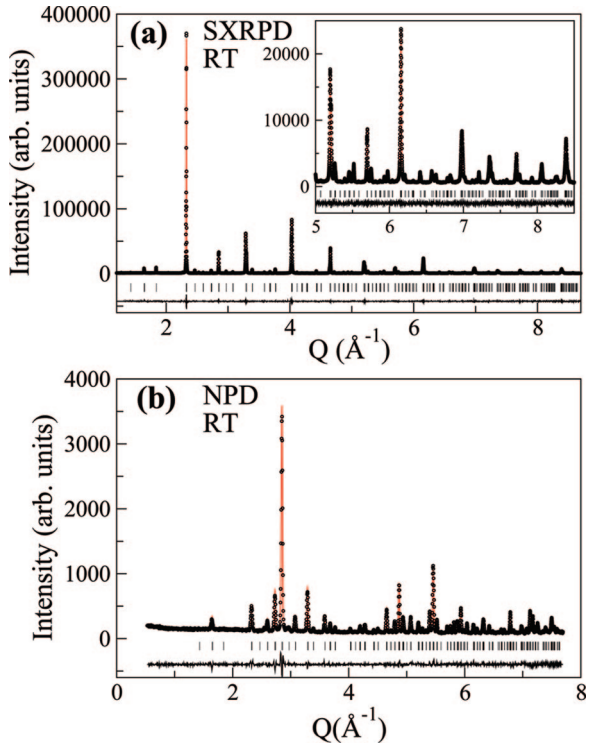

Figure 3. SXRPD (a) and NPD (b) patterns measured at RT jointly refined by the Rietveld method using the *Pnma* space group. The inset in panel (a) shows in detail the high Q region of the SXRPD pattern.

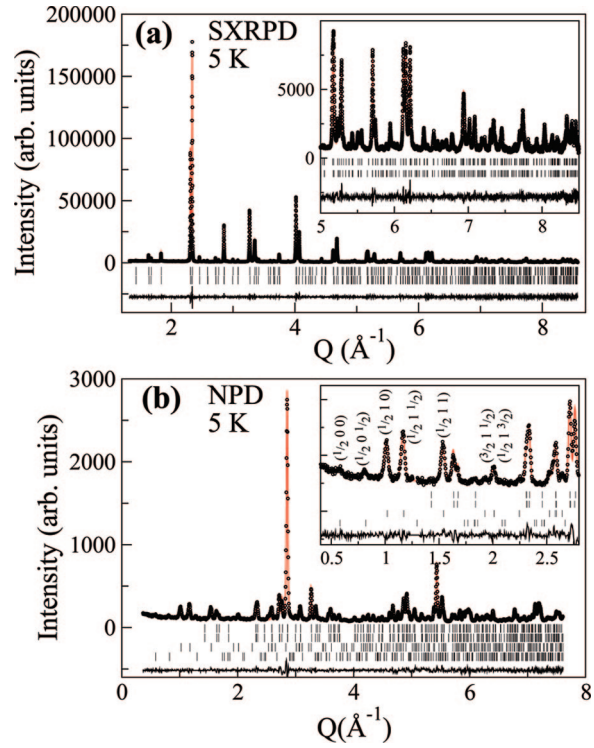

Figure 4. SXRPD (a) and NPD (b) patterns measured at 5 K jointly refined by the Rietveld method. The two phases found are described using *Pnma* space group. The inset in panel (a) shows in detail the high Q region of the SXRPD pattern. The inset in panel (b) shows in detail the low Q region of the NPD pattern where magnetic reflections appear; labels show the indices of these reflections.

as reported for other substituting species like Co,[5] Ga,[6] Ni,[26] and so forth. It must be highlighted that the low field part of the first-magnetization curves shows no evidence of spontaneous ferromagnetism at 2 K. This contrasts with the effect of other substituting ions like Cr, Ni, or Fe, as expected from the fact that Ti^{4+} has no d electrons.[27]

3.2. Microstructure and Coexisting Structures in the Phase Separated State. Figures 3 and 4 show the jointly refined SXRPD and NPD patterns at room temperature (RT) and at 5 K, respectively. We have also collected SXRPD data at different temperatures during the cooling process from RT. In addition, in order to investigate the origin of the differences shown by magnetization and resistivity measurements under heating−cooling cycles, we have also collected SXRPD data at 150 K after heating the sample from 5 K. Results of the Rietveld refinements are summarized in Table 1. It is of relevance to remark that ultra high resolution SXRPD patterns collected at RT and at 250 K can be very well refined ($\chi^2 = 2.6$ and 2.1, respectively) assuming a single phase with the *Pnma* (No. 62) space group. Contrarily, patterns taken at 200 K and below always show the coexistence of two phases (both well described with the *Pnma* space group). For convenience we label these phases as phase-1 and phase-2. In the following we will focus on the most relevant structural and microstructural features observed below the stabilization of an inhomogeneous charge/orbital ordered state below T_{CO}.[11−14] In the case studied here, low Ti doping, the two phases present the type of structural deformation usually found in (single phase) charge-ordered manganites (half-doped): for both phases, a and c lattice parameters are larger than in the high temperature phase while b is shorter. To quantify this cell distortion, we introduce parameter $\xi \equiv 1000 \times \{[(a + c)/(b\sqrt{2})] - 1\}$, which monitors the difference between the basal lattice parameters (a and c) and the apical one (b). This parameter is also printed in Table 1 for the different studied temperatures. According to these data, this deformation is higher in phase-1 than in phase-2, but the difference reduces on cooling.

Previous works on substituted manganites have evidenced the active role of microstrains in phase coexistence.[11,14] Synchrotron diffraction peaks corresponding to phase-2 (small ξ) are considerably wider than those of phase-1. This peak widening is anisotropic, and to properly account for it, we have analyzed experimental peak shapes following the Stephens' formalism for microstrain (see Section 2).[11,19,20] Strain parameters, S_{HKL}, reported in Table 1 monitor the evolution of these microstrains. According to Stephens' formalism S_{400}, S_{040}, and S_{004} account for the fluctuations of a, b, and c lattice parameters respectively while S_{220}, S_{202}, and S_{022} contain information on the correlation of the fluctuations of the lattice parameters. In agreement with previous results,[11,14] microstrains are higher in phase-2, the phase with smaller cell distortion.

First, it is worth discussing in some detail the results obtained when the less distorted phase (phase-2) is the majority one (200 K and 150 K on cooling). In these cases the three strain parameters giving information about the

(26) García-Munoz, J. L.; Bellido, N.; Frontera, C.; Hernández-Velasco, J.; Ritter, C.; Yaicle, C.; Martin, C.; Maignan, A. *J. Appl. Phys.* **2005**, *97*, 10H701.
(27) Hébert, S.; Maignan, A.; Martin, C.; Raveau, B. *Solid State Commun.* **2002**, *121*, 229.

Table 1. Structural Details and Reliability Factors Found by Rietveld Refinement of SXRPD Data (and NPD at 5 K and RT)[a]

			200 K[c]		150 K[c]		5 K[b,c]		150 K[d]	
	RT[b]	250 K[c]	phase-1	phase-2	phase-1	phase-2	phase-1	phase-2	phase-1	phase-2
a (Å)	5.4128(1)	5.4157(1)	5.4336(1)	5.4199(2)	5.4423(1)	5.4291(2)	5.4436(1)	5.4398(5)	5.4432(1)	5.4375(4)
b (Å)	7.6243(1)	7.6130(1)	7.5518(3)	7.5952(3)	7.5200(1)	7.5633(4)	7.5037(1)	7.5351(7)	7.5161(1)	7.5502(6)
c (Å)	5.4014(1)	5.4030(2)	5.4273(1)	5.4081(2)	5.4372(1)	5.4194(2)	5.4385(1)	5.4288(5)	5.4385(1)	5.4254(4)
V (Å^3)	222.91(1)	222.77(1)	222.70(1)	222.62(1)	222.52(1)	222.53(2)	222.15(1)	222.52(4)	222.50(1)	222.74(5)
ξ	2.9	4.9	17.0	8.1	23.0	14.2	25.5	19.9	23.7	17.4
wt %	100	100	21(1)	79(1)	33(1)	67(1)	74(1)	26(1)	73(2)	27(2)
d_{Mn-O1}	1.9435(5)	1.9394(5)	1.924(2)	1.9353(8)	1.9175(15)	1.933(1)	1.916(1)	1.927(3)	1.921(1)	1.928(3)
$\langle d_{Mn-O2}\rangle$	1.948(2)	1.949(2)	1.952(11)	1.951(4)	1.957(8)	1.954(5)	1.957(5)	1.952(16)	1.957(5)	1.962(11)
$\langle d_{Mn-O}\rangle$	1.946(1)	1.946(2)	1.943(8)	1.946(3)	1.944(6)	1.947(4)	1.944(4)	1.944(12)	1.945(4)	1.951(8)
$\theta_{Mn-O1-Mn}$	157.48(2)	157.85(2)	157.9(1)	157.7(1)	157.3(1)	156.1(1)	156.5(1)	155.8(2)	156.0(1)	156.4(1)
$\theta_{Mn-O2-Mn}$	157.93(7)	157.72(9)	159.1(4)	157.6(2)	158.7(3)	157.8(2)	158.7(2)	159.4(7)	158.7(2)	156.2(4)
$\langle\theta_{Mn-O-Mn}\rangle$	157.78(5)	157.76(7)	158.7(3)	157.6(2)	158.2(3)	157.2(2)	158.0(2)	158.2(5)	157.8(2)	156.3(3)
S_{400}	0.39(1)	0.37(1)	0.66(1)	1.60(2)	0.08(1)	2.21(2)	0.09(1)	2.60(17)	0.13(1)	3.05(17)
S_{040}	0.16(1)	0.21(1)	0.39(1)	1.23(1)	0.15(1)	2.47(2)	0.18(1)	3.21(10)	0.17(1)	2.76(11)
S_{004}	0.37(1)	0.35(1)	0.85(2)	1.89(2)	0.19(1)	3.85(4)	0.47(1)	2.81(20)	0.41(1)	2.80(18)
S_{220}	-0.06(1)	−0.13(1)	0.14(2)	−1.69(2)	−0.07(1)	−2.31(4)	−0.04(1)	−0.91(40)	0.01(1)	−1.25(29)
S_{202}	1.58(1)	1.50(2)	1.02(3)	5.14(4)	0.57(1)	7.39(6)	1.33(1)	3.98(33)	0.93(1)	7.79(34)
S_{022}	−0.14(1)	−0.21(1)	−0.89(2)	−1.80(3)	−0.19(1)	−3.78(5)	0.37(1)	1.18(46)	0.33(1)	0.18(31)
R_B	1.8[e] 5.2[f]	2.38	2.6	2.0	2.0	2.7	2.3[e] 4.9[f]	3.4[e] 5.5[f]	2.1	3.2
χ^2	2.6[e] 1.2[f]	2.1	3.1		3.6		3.18[e] 4.52[f]		3.5	

[a] All refinements have been done using the *Pnma* space group. O1 stands for apical oxygen in Wyckoff position 4c and O2 for basal oxygen in 8d. Parameter $\xi \equiv 1000 \times \{[(a + c)/(b\sqrt{2})] - 1\}$ is also shown. [b] From the joint refinement of NPD and SXRPD data. [c] Measured after cooling from RT. [d] Measured after heating from 5 K. [e] Reliability factors for SXRPD pattern. [f] Reliability factors for NPD pattern.

correlations between fluctuations of cell parameter (S_{220}, S_{202}, and S_{022}) are quite revealing. For phase-2, S_{220} and S_{022} are negative, which means that a compressive (expansive) fluctuation of b is, on average, accompanied by an expansive (compressive) fluctuation of a and c. In contrast S_{202} is positive signaling that the fluctuations of a and c point in the same direction. It is worth recalling that during the cell distortion taking place at T_{CO} a and c evolve in the same direction while b does in the opposite direction. We thus observe that cell fluctuations (microstrains) mimic the cell distortion taking place at T_{CO}. So, in phase-2 (and at 200 K and 150 K on cooling), the fluctuations of a, b, and c cell parameters, giving rise to the anisotropic peak broadening, occur in a correlated manner ($\Delta a \sim \Delta c \sim -\Delta b$) giving rise to well defined fluctuations of the ξ parameter. This parameter monitors the cell distortion produced by charge localization in the $a-c$ plane due to orbital ordering, related with the localization and ordering of the charges. Therefore, we deduce that peak broadening in phase-2 is produced by fluctuations in the concentration of orbital ordered cells or, equivalently, that phase-2 presents very significant fluctuations of the concentration of defects in the COO matrix.

Thus, the scenario in this temperature range is the coexistence of two phases, one with strong and well defined cell distortion, ξ parameter, and the second with a smaller mean cell distortion and high fluctuations around its mean value.

On further cooling, at 5 K, phase-1 becomes the majority (∼75 wt %) and the ξ parameter of phase-2 grows to a value comparable to that of phase-1 (in contrast with the values obtained at 150 K on cooling). Accompanying these changes the strain parameters, especially those directly related with the correlations between cell parameters fluctuations, decrease quite drastically and lose the correspondence to ξ fluctuations.

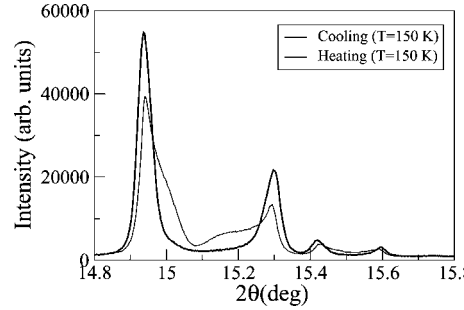

Figure 5. Detail of the SXRPD collected at $T = 150$ K after cooling from RT (cooling) and after heating from 5 K (heating).

Figure 5 illustrates the differences between SXRPD data taken at 150 K after cooling from RT and after heating from 5 K. The large differences that can be appreciated are clearly reflected in values reported in Table 1. In fact, the main difference relies on the fraction of the two coexisting phases. Relative fractions and the rest of the structural parameters do not change significantly on heating the sample from 5 K to 150 K. Thus, the difference in the distortion ξ of the two phases is smaller when heating from 5 K. In addition, we do not observe well defined fluctuations of ξ parameter in phase-2 on heating; meanwhile, the CO matrix (phase-1) is clearly the dominant phase.

As a result of these observations we must ascribe the different values of the magnetization found at 150 K to the difference in phase fractions. Thus, the second transition observed in the magnetization curve between 150 K and 100 K (on cooling) is produced by the transformation of an important fraction of the system (∼40 wt %) from phase-2 to phase-1. Accompanying this transformation, the remaining phase-2 becomes more similar to phase-1: more distorted and less strained. This structural transformation is not reversed on heating, giving rise to the hysteresis in the

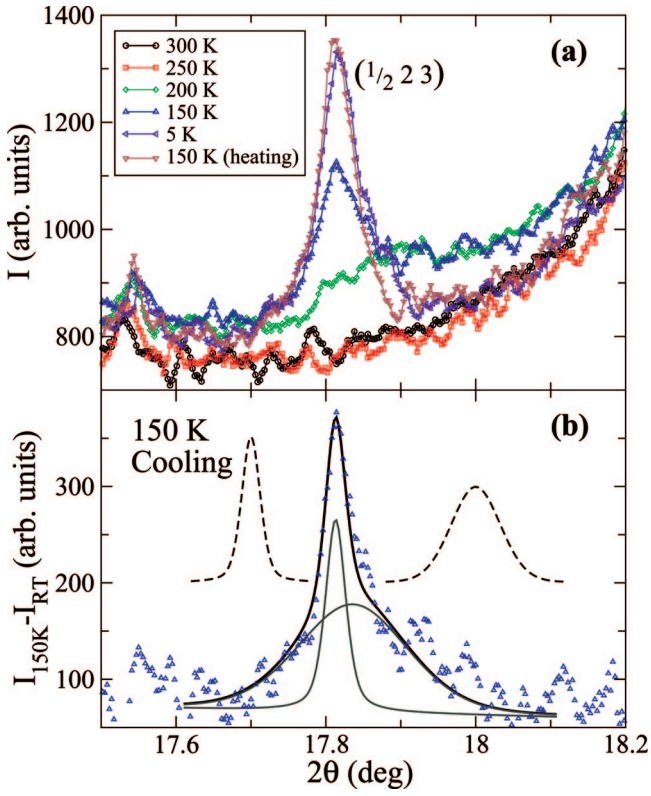

Figure 6. (a) Temperature evolution of the superstructure peak ($^1/_2$ 2 3). (b) Fitting of the difference between the intensities found at 150 K (after cooling) and at RT, to a sum of two pseudo-Voigt functions as explained in the text. Dashed lines in panel (b) show the peak shapes expected for phase-1 (left) and phase-2 (right) from strain-only broadening as explained in the text.

cooling−heating process in magnetization and resistivity measurements.

3.3. Short-Range Orbital Ordered Domains. One manifestation of orbital order (OO) in half-doped manganites is the appearance of a structural modulation that doubles one lattice parameter. We have found several small peaks in the SXRPD patterns collected below T_{CO} that can be indexed by doubling the *a* lattice parameter. It is well-known that these small superstructure reflections should be attributed to the periodic arrangement of occupied e_g orbitals characterized by a wave vector $q^k = (\delta, 0, 0)$ where the wavenumber δ corresponds to the inverse of the orbital period (in lattice cell units). Within our instrumental limitation, we did not detect clear incommensurate reflections but well defined $\delta \simeq 1/2$ superstructure peaks. Figure 6a shows one of these superstructure reflection at different temperatures. In this figure, it can be appreciated how this small reflection (its is $\sim 3 \times 10^{-3}$ times the most intense peak) evolves with the temperature. At RT and 250 K it has not appeared yet. At 200 K, clearly, a small and wide bump is appreciated. It is of interest to notice in this figure that the signal at 150 K (after cooling) is composed of a well defined peak plus a bump not very different to that found at 200 K. The position of this peak perfectly coincides with the position of ($^1/_2$ 2 3) superstructure reflection of phase-1. We call attention to the presence of the wide bump, which probes the existence of OO domains of small size.

The high angular resolution of ID31 has permitted us to evaluate the characteristic sizes of the distinct OO domains. To quantify these sizes, it is necessary to estimate the FWHM of the small bump and of the peak. This can be done by fitting the intensity to a sum of two peaks, centered at positions corresponding to ($^1/_2$ 2 3) superstructure reflections of the two phases. Unfortunately, these reflections are superimposed to the tail of the (3 2 1) reflection. To take this into account we have subtracted from the intensity measured at 150 K (on cooling) that which was measured at RT. The signal obtained has been fitted to the sum of two pseudo-Voigt functions at fixed positions [those given by ($^1/_2$ 2 3) reflections of phase-1 and phase-2]. The result is plotted in Figure 6b. The FWHMs obtained have been compared with those expected from the strain parameters printed in Table 1 (transformed accordingly to the doubling of *a* lattice parameter). Peak shapes expected from strain only broadening are plotted as dashed lines in Figure 6b. The measured FWHMs are larger than the calculated ones without considering size effects. Thus, in addition to anisotropic peak broadening, peak shape also reflects the finite size of the diffracting regions. Introducing in the analysis the effect from finite coherence length of the OO domains, we have obtained very different characteristic lengths in the two phases: 1000 Å for phase-1 and around 200 Å for phase-2.

At 5 Kthe peak has grown considerably, and the bump around it has disappeared almost completely. At 150 K after heating, the intensity is very similar to that found at 5 K, with a quite intense peak. At 150 K (after cooling) phase-2 represents 2/3 of the sample and only 1/3 of the cells adopt the structure of phase-1. In contrast, at 5 K and at 150 K (after heating) phase-2 represents only 1/4 of the sample. Thus, we must assume that the intensity of the narrow superstructure peaks in Figure 6 is predominantly generated at the phase-1 regions whereas the much wider peak (bump) tell us that OO domain of hundreds angstroms (tens of nanometers) in size are very common in phase-2 regions. Thus, in connection with the second transition observed in the $M(T)$ curve around 140 K (on cooling), our diffraction data establish that this transition is due to the spontaneous transformation of a huge fraction of the system (near 40 wt %) from phase-2 to phase-1. At the same time, Figure 6 shows a redistribution of the diffracted intensity from OO domains: most of the intensity coming from short-range OO domains (bump, phase-2) is transferred to the narrow OO peak (long-range OO regions, phase-1). As a result, the intensity of the narrow ($^1/_2$ 2 3) superstructure peak has doubled below the transition.

Thereby, we are led to the conclusion that the thermal irreversibility has its origin in the formation of metastable glass-like OO domains with a characteristic coherence length of ~200 Å in $Pr_{0.50}Ca_{0.50}Mn_{0.99}Ti_{0.01}O_3$. Quenched disorder and strain seem to be key elements to stabilize the variable-range phase coexistence, out of thermodynamical equilibrium in $Pr_{0.50}Ca_{0.50}Mn_{1-x}Ti_xO_3$ with low substitution by d^0 cations. In this context, it is interesting to recall that, accompanying

Table 2. Magnetic Structures Found by Refining the Low Temperature NPD Pattern[a]

Phase-1, CE ($\mu_y = \mu_z = 0$, $R_M = 8.0$)	
atomic positions	$\mu_T = \mu_x$ (μ_B)
($^1/_4$, 0, 0) ($^1/_4$, 0, $^1/_2$) ($^3/_4$, $^1/_2$, 0) ($^3/_4$, $^1/_2$, $^1/_2$)	1.58(8)
($^3/_4$, 0, 0) ($^3/_4$, 0, $^1/_2$) ($^1/_4$, $^1/_2$, 0) ($^1/_4$, $^1/_2$, $^1/_2$)	−1.58(8)
(0, 0, $^1/_4$) ($^1/_2$, 0, $^3/_4$) ($^1/_4$, $^1/_2$, $^1/_4$) (0, $^1/_2$, $^3/_4$)	1.37(8)
($^1/_2$, 0, $^1/_4$) (0, 0, $^3/_4$) (0, $^1/_2$, $^1/_4$) ($^1/_2$, $^1/_2$, $^3/_4$)	−1.37(8)

Phase-2, Pseudo-CE ($\mu_z = 0$, $\mu_T = 1.4(2)\mu_B$, $R_M = 17.0$)		
atomic positions	μ_x (μ_B)	μ_y (μ_B)
($^1/_4$, 0, 0) ($^1/_4$, 0, $^1/_2$) ($^1/_4$, $^1/_2$, 0) ($^1/_4$, $^1/_2$, $^1/_2$)	1.0(3)	1.0(2)
($^3/_4$, 0, 0) ($^3/_4$, 0, $^1/_2$) ($^3/_4$, $^1/_2$, 0) ($^3/_4$, $^1/_2$, $^1/_2$)	−1.0(3)	−1.0(2)
(0, 0, $^1/_4$) ($^1/_2$, 0, $^3/_4$) (0 $^1/_2$, $^1/_4$) ($^1/_2$, $^1/_2$, $^3/_4$)	1.0(3)	1.0(2)
($^1/_2$, 0, $^1/_4$) (0, 0, $^3/_4$) ($^1/_2$, $^1/_2$, $^1/_4$) (0, $^1/_2$, $^3/_4$)	−1.0(3)	−1.0(2)

[a] The refinement has been done by assuming CE-magnetic order in phase-1 and pseudo-CE magnetic order in phase-2. Atomic positions are related to the magnetic cell found to be given by $a_M = 2a$, $b_M = b$, and $c_M = 2c$.

the partial phase transformation at ∼140 K, phase-2 (now the minority) becomes more similar to phase-1: more distorted and less strained (Table 1).

3.4. Magnetic Structures and Range of Magnetic Order. From the low angle region of the NPD pattern collected at 5 K we have gained information about the magnetic state in the two structural phases. The most intense magnetic peaks are shown, together with corresponding indices (referred to as the *Pnma* cell) in the inset of Figure 4b. Our d^0 impurity ions do not favor the formation of ferromagnetic islands, and only AFM peaks have been detected. In accordance with the two structural phases, two distinct sets of magnetic reflections are identified which correspond, respectively, to CE and pseudo-CE magnetic domains. Magnetic intensities corresponding to pseudo-CE order [with *k*-even in the inset of Figure 4b] are less intense than those generated at CE-type magnetic domains (*k*-odd). This agrees with the fraction of the robust COO phase (commonly showing CE AFM order) being almost 3 times the fraction of the less distorted phase-2 at the same temperature (5 K). Consistently, pseudo-CE magnetic regions must be attributed to domains/clusters richer in Ti^{4+} that favor the unbalance of Mn^{3+}/Mn^{4+} ions.

Table 2 summarizes the details of the two magnetic structures found at 5 K, refined using the structural details obtained by the joint analysis of NPD and SXRPD data. By assuming that phase-2 stabilizes preferentially around Ti^{4+} ions, for magnetic refinements we ascribed CE magnetic structure to phase-1 and pseudo-CE order to phase 2 (the inverse leads to unrealistic moments, larger than 4.5 μ_B, for Mn in phase-2). The best refinement of the former is obtained with magnetic moments parallel to the *a*-axis. It is true, however, that due to the similarity of *a* and *c* parameters, atomic positions and moment directions in Table 2 can be turned 90° with no appreciable changes in agreement parameters. The small signal coming from pseudo-CE domains was well reproduced using the same moment for all Mn positions, the main feature being an out of plane component of the ordered moments very similar to that in the *a*−*c* plane. It must be mentioned that, due to the small magnetic signal, we have restricted ourselves to collinear magnetic structures.

Although the substitution level is very low, the shape of CE magnetic peaks does not exhibit the characteristic splitting of magnetic coherence lengths coming from magnetic twin boundaries as found in pure (La or Pr)$_{0.5}$Ca$_{0.5}$MnO$_3$.[28] The reason is that CE (and also pseudo-CE) magnetic domain sizes are rather small. Both CE and pseudo-CE reflections are significantly broadened. Their broadening has been analyzed using isotropic size broadening Lorentzian approximations. We obtained a very similar magnetic domain size of ∼200 Å for CE and pseudo-CE structures.

The small CE domain size found (∼200 Å) contrasts with the characteristic coherence length (∼1000 Å) of the OO domains in phase-1, but it is similar to the size of the magnetic domains found in pure $Ln_{0.5}Ca_{0.5}MnO_3$. This effective size of the magnetic domain is attributed to the formation of antiphase domain boundaries (as illustrated by Radaelli et al.[28]). On the other hand, it is of interest to notice in Table 2 that the ordered magnetic moments of both phases (1.4−1.6 μ_B) are very low with respect to fully polarized Mn moments (3−4 μ_B). This proves a great degree of magnetic disorder in the whole system: in pseudo-CE but also in CE domains (due to the presence of Ti in both phases). Values of the ordered magnetic moments significantly smaller than the full polarization of Mn have also been reported for other Mn-substituted compounds like Al[29] and Ga (both d-less)[13] or Co (with d electrons).[11]

It is worth mentioning that a minority fraction of pseudo-CE magnetic intensity might come as well from small defective regions within the phase-1, due to the presence of some Ti atoms. But this possibility does not change the conclusions of our analysis: there is a large degree of magnetic disorder in phase-2 and phase-1 regions.

4. Summary and Conclusions

To summarize, we have carefully characterized the lowly substituted $Pr_{0.50}Ca_{0.50}Mn_{0.99}Ti_{0.01}O_3$ compound, in order to gain insight in the phase separation phenomena generally found in $Pr_{0.50}Ca_{0.50}Mn_{1-x}M_xO_3$ family. As a starting result, we have found clear differences between its properties on cooling and on heating in a wide temperature range. These differences start, on cooling at $T_{CO} \simeq 240$ K, the temperature when the parent $Pr_{0.50}Ca_{0.50}MnO_3$ compound presents the charge ordering transition, and extend down to $T \simeq 100$ K. We have confirmed that this behavior (thermal hysteresis below T_{CO}) is reproducible for differently synthesized samples. Interestingly, this behavior is not exclusive of Ti substitution. It seems to be associated with low doping levels, because previously published macroscopic studies on $Pr_{0.50}Ca_{0.50}Mn_{0.99}Cr_{0.01}O_3$ and $Pr_{0.50}Ca_{0.50}Mn_{0.975}Al_{0.025}O_3$ report this behavior, [23,24] and we have further found it on $Pr_{0.50}Ca_{0.50}Mn_{0.995}Ni_{0.005}O_3$ and $Pr_{0.50}Ca_{0.50}Mn_{1-x}Ru_xO_3$ ($x =$ 0.005 and 0.01).

By means of ultrahigh resolution SXRPD we have carefully characterized the structural evolution of $Pr_{0.50}Ca_{0.50}Mn_{0.99}Ti_{0.01}O_3$ with special interest in the differ-

(28) Radaelli, P. G.; Cox, D. E.; Marezio, M.; Cheong, S.-W. *Phys. Rev. B* **1997**, *55*, 3015.
(29) Martin, C.; Maignan, A.; Damay, F.; Hervieu, M.; Raveau, B.; Jirak, Z.; Andre, G.; Bouree, F. *J. Magn. Magn. Mater.* **1999**, *202*, 11.

ences found in the cooling−heating cycle. This study reveals that at $T_{CO} \simeq 240$ K the system presents a transition from a single phase ($T > T_{CO}$) to a coexistence of two different phases ($T < T_{CO}$) both presenting charge/orbital order. The detailed structural and microstructural characterization points out that, after cooling through this transition, one of these phases (phase-1) presents a robust and well defined COO, characterized by a high distortion of lattice parameters (monitored through ξ parameter) and a small lattice strain. In contrast the other phase (phase-2) presents a smaller degree of lattice distortion and much higher lattice strain. The analysis of strain broadening of the very high resolution SXRPD data has allowed us to conclude that this strain corresponds to well defined fluctuations of the lattice distortion. Thus, phase-2 presents less distortion with high fluctuations around its mean value. This must be ascribed to the appearance of fluctuating charge/orbital order in this phase. The evidence of orbital ordering in both phases is reinforced by the presence of small superstructure peaks in SXRPD patterns. These superstructure peaks clearly reveals different characteristic domain sizes. The shape of these small reflections prove a coherence length of OO considerably larger in phase-1 (1000 Å, as expected for a polycrystalline Manganite) than in phase-2 (200 Å). Consequently, we can conclude that phase-2 presents short-ranged orbital order, in accordance with its fluctuating COO state. The thermal hysteresis that we have found in macroscopic properties and structural details makes us conclude that this second phase is not a well defined equilibrium phase but just a metastable state.

The second transition (on cooling), related with the weakening of the metastable state, evidenced by macroscopic measurements, is also accompanied by remarkable structural changes. It corresponds to a partial transformation of phase-2 into phase-1 (which becomes the majority phase at low temperature). Thus, on cooling below 100−140 K, an important fraction of phase-2 develops well defined charge/orbital order becoming phase-1. In addition, the distortion of the remaining phase-2 increases to values more similar to those obtained for phase-1, and its strain reduces, indicating that the glassiness of this phase reduces after this second transition, decreasing as its own phase fraction is reduced.

NPD data reveal that, in accordance with the structural distortions found and the presence of small superstructure peaks, the coexisting phases both present antiferromagnetic order. This is also reinforced by the isothermal $M(H)$ curve, at low temperature, showing a total absence of ferromagnetic signal. NPD data show the coexistence of two magnetic structures: CE and pseudo-CE. As a very likely scenario, we have assigned the former to phase-1 and the latter to phase-2. The ordered magnetic moments are very similar in both phases and much smaller than that corresponding to fully polarized Mn ions. This indicates the presence of magnetic disorder at low temperatures. The size of the magnetic domains was found to be only slightly lower than in $Ln_{0.5}Ca_{0.5}MnO_3$,[28] where the size is determined by the presence of antiphase domain boundaries.

As mentioned before, remarkable thermal hysteresis has been also been observed in macroscopic measurements [$M(T)$, $\rho(T)$] of other $Pr_{0.50}Ca_{0.50}Mn_{1-x}M_xO_3$ systems at very low doping levels. Research presented here provides a microscopic picture for the origin of this appealing hysteresis. In addition present work helps to clarify the origin of microstrains by interpreting them as fluctuations of structural distortions produced by orbital ordering.

Acknowledgment. We are thankful for financial support from MEC (Spanish government) under Project Nos. MAT2006-11080-C02-02 and NANOSELECT CSD2007-00041 and Generalitat de Catalunya under Project No. 2005-GRQ-00509. FAME European Network of Excellence is also acknowledged. European Synchrotron Radiation Facility and Institut Laue Langevin are acknowledged for the provision of synchrotron and neutron beam time, respectively.

CM703513T